EU Horizon 2020 Research & Innovation Program
Digital transformation in Health and Care
SC1-DTH-06-2020
Grant Agreement No. 101016496

SimCardioTest - Simulation of Cardiac Devices & Drugs for in-silico Testing and Certification

Technical Report

D3.2: Fluid simulations with optimised boundary conditions

Work Package 3 (WP 3)

Use Case 2 - Left Atrial Appendage Occluder

Task Lead: SRL, NO

WP Lead: UPF, SP

PUBLIC

DELIVERABLE INFORMATION

Deliverable number	D3.2
Deliverable title	Fluid simulations with optimised boundary conditions
Description	Sensitivity analyses of relevant parameters for realistic fluid simulations
Lead authors	Ehsan Khalili
Contributors	Kristian Valen-Sendstad, Oscar Camara, Andy Luis Olivares, Jordi Mill, Henrik Kjeldsberg, Carlos Albors, Hermenegild Arevalo
Due date	M18
Submission date	30 June 2022 as confidential 16 June 2023 as PUBLIC
Comments	The first version submitted at M18 was confidential as a publication on the work was planned. The publication being under review (at the International Journal for Numerical Methods in Biomedical Engineering), we submit the deliverable at M30 a PUBLIC

Document history			
Date	**Version**	**Author(s)**	**Comments**
15/06/2022	V1	E. Kahili	Feedback Alessia Baretta
23/06/2022	V2	E. Kahili	Final
15/11/2022	V3	M. Barbier	Format editing
16/06/2023	VF	M.Barbier	Public version

Table of Contents

EXECUTIVE SUMMARY

Non-valvular atrial fibrillation, the most common sustained cardiac rhythm disturbance in Europe, disturbs the normal behaviour of the heart and creates the appropriate environment to generate thrombus. Computational fluid dynamics (CFD) is rapidly gaining ground as a powerful non-invasive approach to evaluate dynamical behaviour of blood flow in the left atrium. Systematic verification and validation studies, following the ASME V&V40 guidelines with in-vitro and/or ex-vivo data, is a need for building credibility of in-silico models to integrate them as part of the medical device certification procedures. This report defines a sensitivity analysis of different CFD options such as spatial resolution, mesh boundary layers, solver robustness, as well as boundary condition scenarios available in the literature to identify the optimal modelling choices for predicting hemodynamic indices and subsequently thrombus formation particularly device-related thrombus (DRT). The results signify that it is crucial to perform proper verification studies to reach solver settings, spatial and temporal resolutions that can uncritically be applied to any given case. Moreover, patient-specific data as much as possible is needed to personalise the fluid models, especially velocity/pressure waveforms at the PV/MV and LA wall deformation.

1 - Introduction

With the worldwide ageing of the population characterised by a large influx of "baby boomers", an AF epidemic is forecasted within the next 10 to 20 years (Aronow & Banach, 2009), with a significant amount of health resources being invested in detecting and managing AF. The majority of deaths related to cardiovascular disease (85%) are due to heart attack and stroke, with cardiogenic emboli being the causative factor in 20% to 40% of all stroke cases (Hur et al., 2011). Non-valvular atrial fibrillation, the most common sustained cardiac rhythm disturbance in Europe, disturbs the normal behaviour of the heart and creates the appropriate environment to generate thrombus, the so-called Virchow's triad (e.g. hypercoagulability, haemodynamics changes, and endothelial injury dysfunction). Around 99% of AF-related strokes originate from thrombus formed in a cavity of the left atrium (Cresti et al., 2019), the left atrial appendage (LAA). Since AF causes a deceleration of blood flow, a stasis can occur, increasing the risk of thrombus formation in the LAA. The thrombus can loosen and be transported through the circulatory system to the brain, causing a cardioembolic stroke.

Until recently, the main therapeutic solution to treat cardioembolic accidents was based on oral anticoagulation (OAC) therapy, usually prescribed on those AF patients over 65 years old. During the past 20 years, left atrial appendage occlusion (LAAO) devices have been developed as an alternative when oral anticoagulation (OACs) are not appropriate, due to high risk of bleeding or because of patient limitations. A meta-analysis (Whang, 2018) combining five-year outcome data from the two published randomised clinical trials on LAAO devices, PROTECT AF and PREVAIL, confirmed the non-inferiority of Watchman LAAO devices from Boston Scientific with respect to oral anticoagulants for the composite of stroke, systemic embolism and cardiovascular/unexplained death, while showing better outcomes on mortality, haemorrhagic stroke and major bleeding. However, there are still important questions on the selection of the right device for a given patient as well as the optimal positioning. In-silico trials on such devices can provide crucial mechanistic insights thanks to the details of computational fluid dynamics simulation.

Computational fluid dynamics (CFD) constitutes a powerful non-invasive approach to determine physically meaningful indicators for evaluating dynamical behaviour of blood flow in the left atrium. Numerical simulation studies for Atrial fibrillation (AF) are increasingly sophisticated. Most of these studies focused on analysing in-silico haemodynamics parameters in the LAA in relation to thrombogenic risk, including explicit models of thrombus formation (Qureshi et al., 2020, Wang et al., 2020). The influence of pulmonary vein configuration on blood flow patterns in the LA, was also studied (Dahl et al., 2012, García-Isla et al., 2018, Fang et al., 2021, Mill, Harrison, et al., 2021). In addition, the effect of LAA closure has been modelled (Zhang & Gay, 2008, Jia et al., 2019, D'Alessandro et al., 2020), the most advanced investigations having incorporated LAAO devices (Aguado et al., 2019, D'Alessandro et al., 2020) and the relation thereof to device-related thrombus (DRT).

The mentioned works use a wide range of boundary conditions and of modelling choices in terms of inlet/outlet set up (e.g., velocities and pressures in the pulmonary veins and mitral valve; from literature or patient-specific), LA wall behaviour (e.g., rigid, modelled dynamic mesh or deformation from medical images, fluid-structure interaction), and mesh resolution (e.g., from 0.4 to 3 $x10^5$ mesh elements), among other factors. Table 1 shows a summary of the corresponding modelling strategies reported in the literature. Unfortunately, the absence of joint benchmark studies with reliable ground-truth makes it difficult to identify which are the optimal configurations to achieve

realistic simulations. Moreover, there is no consensus on the most appropriate metrics for the quantification of blood flow simulations. Most studies report velocity profiles in relevant points of interest (e.g., filling/emptying velocities in the LAA), typically complemented with estimations of time-averaged wall shear stress (TAWSS), oscillatory index (OSI), endothelial cell activation potential (ECAP), residence times (TR), shear strain rate (SSR), kinetic energy (KE), particle tracking/residence analysis and vortex visualisation with the Q-criterion or the Lambda2 metrics. Qualitative analyses of the blood flow patterns with streamline-based visualisation are commonly included. Arguably, the published investigations are usually based on only a few (<10) sets of patient-specific LA geometries (see Table 1). Due to the extensive range of modelling options reported in LA computational fluid dynamics, there is a need for best-practice guidelines to build robust models and optimise boundary conditions in order to achieve reliable simulations as regards relevant clinical outcomes in LAAO (Mill et al., 2021).

Systematic verification and validation studies, following the ASME V&V40 guidelines (Viceconti et al., 2021) with in-vitro and/or ex-vivo data, are also missing due to the difficulties to obtain ground-truth data. Therefore, there is a need for building credibility of in-silico models to integrate them as part of the medical device certification procedures by organisms such as the Food and Drug Administration (FDA). The goal of this study was to outline the blood flow modelling choices and perform sensitivity analysis to determine optimal methodological choices in fluid simulations in LA fluid modelling for the prediction of dynamical behaviour of blood flow and thrombus formation. We systematically studied spatial resolutions, mesh boundary layers and numerical strategy in the context of spatial and temporal resolutions. Moreover, a sensitivity analysis of several boundary conditions scenarios, varying inlet/outlet and LA wall movement configurations, using LAAO patient-specific data in the context of DRT, was performed.

Table 1. Summary of boundary conditions and different modelling choices for left atrial fluid simulations reported in the literature. PV: Pulmonary veins; MV: mitral valve; Geoms: number of geometries; vels: velocities; press: pressures; dCT/MRI: dynamic Computed Tomography / Magnetic Resonance Imaging; Diff. DM: diffusion-based dynamic mesh; FSI: fluid-structure interaction;
** Synthetic LA and realistic LAA geometries;*
*** Estimated value from element size reported in the paper;*

**** 256 synthetic and 114 real LAA.*

Authors (year)	PV inlet BC	MV outlet BC LV systole/diastole	Wall behaviour	Mesh elements (millions)	Cohort
Zhang & Gay, 2008	Lit. Vels.	Wall / 0 mmHg	FSI	0.2	1
Dahl et al., 2012	Patient flow	Added mass flux	Rigid	2.1	1
Koizumi et al., 2015	10 mmHg	Wall / 8 mmHg	dMRI	0.16	1
Otani et al., 2016b	dCT Vels.	wall / dCT flow	dCT	0.36-0.5	2
Bosi et al., 2018	0 mmHg	Generic vels.	Rigid	2.2-3.0	4
García-Isla et al., 2018	Generic vels.	Wall / 8 mmHg	Rigid	0.35-0.5	36 *
Dillon-Murphy et al., 2018	0 mmHg	dMRI flow	dMRI	17**	2
Morales et al. 2018	Generic vels.	Wall / 8 mmHg	Diff. DM	0.35-0.9	370 ***

Masci et al., 2019a	Flow balance	Generic flow	Sinusoidal	1.7-1.9	5
Aguado et al., 2019	Generic vels.	Wall / 8mmHg	Rigid	0.2-0.96	2
Jia et al., 2019	Synthetic vels.	Wall / 0mmHg	Rigid	0.04-0.06	1
Feng et al., 2019	Generic press.	Generic press.	FSI	0.1	1
Masci et al., 2019	Flow balance	Generic flow	Sinusoidal Rigid	0.8-0.1	2
Wang et al., 2020	10 mmHg	Generic flow	Rigid	2.4-4.9	1
Mill et al. 2020a	Generic vels.	Wall / 8 mmHg	Diff. DM	0.5	2
D'Alessandro et al., 2020	Flow balance	Generic vels.	Sinusoidal MRI	1.7-1.9	2
Qureshi et al., 2020	Synthetic vels.	Unknown	dMRI	0.4	2
García-Villalba et al., 2020	Flow balance	Wall / Open	Rigid / dCT	16.7 **	6
Fang et al., 2021	AF vels.	Wall / 0mmHg	FSI	Unknown	1 *
Sanatkhani et al., 2021	Generic vels.	Open / 0 mmHg	Rigid	0.35-0.5	16
Mill, et al., 2021b	AF press.	AF vels.	Diff. DM	0.8-0.9	52
Mill et al., 2021c	AF press.	Personalized vels.	Rigid/ Diff. DM	1-5	6
Vella et al., 2021	Constant press.	press. difference	Rigid/DM	2.8-4.5	2
Paliwal et al., 2021	generic vels	Constant pressure	DM	3-8	4
Dueñas-Pamplona et al., 2021b	AF vels.	Constant pressure	Rigid/dCT	0.82-10	2
Corti et al., 2022	Flow balance / mean press	Constant pressure	Diff. DM	Unknown	4

2 - Sensitivity analysis

2.1 - Fluid modelling pipeline

The term patient-specific modelling refers to the construction of 3D models derived directly from patient image data. Models are typically constructed from computed tomography (CT) or magnetic resonance imaging (MRI) data, including detailed anatomy with multiple pulmonary veins and outlet. Although CT or MRI data are typically used, ultrasound and angiography data can provide an attractive alternative as well. Image data are typically segmented with 2D or 3D level set or thresholding methods using open source packages such as vmtk (http://www.vmtk.org/), SimVascular (http://simtk.org) or ITK-SNAP or commercial packages such as Mimics (Materialise, Leuven, Belgium). Image-segmentation methods are a challenging component of the modelling process, often requiring extensive user intervention and manual segmentation when automated methods fail.

Boundary conditions are key to properly model the dynamics of flow and hemodynamics. Boundary conditions for simulations need to be derived from two-dimensional (2D) echocardiography or 4D phase-contrast MRI measurements of flow or dynamic CT scans which are particularly challenging to obtain and rely on. Patient specific boundary conditions particularly at PVs are rarely available

since static-based information is typically accessible, therefore, generic boundary conditions/ waveforms are usually being used instead of subject-specific ones.

2.2 - In-silico haemodynamic indices

Several indices derived from wall shear stress are basically associated with blood stasis such as time-averaged wall shear stress (TAWSS), oscillatory shear index (OSI), relative residence time (RRT) and ECAP. Recent studies have used these indices for atrial flow simulation, relating them to coagulation risk in the LAA (Dueñas-Pamplona et al., 2021). The definitions of these four indices can be found in Table 2.

Table 2. Hemodynamic indices studied in the present work.

Quantity	Abbreviation/Symbol	Definition	Unit
Time averaged wall shear stress	TAWSS	$\frac{1}{T}\int_0^T \lvert\tau\rvert\, dt$	[Pa]
Oscillatory shear index	OSI	$\frac{1}{2}\left(1-\frac{\left\lvert\int_0^T \tau\, dt\right\rvert}{\int_0^T \lvert\tau\rvert\, dt}\right)$	[-]
Relative residence time	RRT	$\frac{1}{(1-2\cdot \mathrm{OSI})\cdot \mathrm{TAWSS}}$	[1/Pa]
Endothelial cell activation potential	ECAP	$\frac{\mathrm{OSI}}{\mathrm{TAWSS}}$	[1/Pa]

2.3 - Sensitivity studies

2.3.1 - Mesh convergence study

2.3.1.1 Introduction

Determining whether a mesh is suitable for a computed flow typically involves one of two possible approaches. The first is to compare numerical solutions with available experimental data (Marsden, 2014), and the second is to compute solutions on very high-resolution meshes. The latter approach for assessing suitability is to employ a series of meshes to demonstrate mesh-independence, which typically leads to a higher computational cost for realistic 3D models. A variant of this approach is to use a mesh which is considered to be large enough. However, in the absence of a systematic methodology for quantifying the solution error, it is unlikely to guarantee the suitability of such large meshes and the resulting accuracy of the numerical methods (Valen-Sendstad & Steinman, 2013). Inasmuch as, demonstration of mesh independence is time-consuming and computationally expensive, and consequently, suitable mesh convergence studies are rarely reported in the computational hemodynamics literature.

2.3.1.2 Methodology

A clinical cohort of 12 models was provided by Hôpital Haut-Lévêque (Bordeaux, France) where Cardiac CT studies were performed on a 64-slice dual source CT system (Siemens Definition, Siemens Medical Systems, Forchheim, Germany). Further details can be found in (Mill et al., 2021a). The twelve geometries were selected to capture LA variability in morphology and morphological phenotype, as quantified based on left atrial appendage (LAA) and LA volumes, their corresponding ratio, the number of pulmonary veins and different types of LAA morphology.

The grid convergence was systematically studied by employing six different meshes varying from 100 thousand to 26 million of tetrahedral elements (i.e. 100k, 400k, 800k, 3.2M, 6.4M and 26M tetrahedral elements). The maximum length for the tetrahedron edge was considered differently for the whole domain including LA and LAA. Therefore, the mesh was refined based on surface curvature to capture the topology of the geometry in order to accurately resolve the important features and zones, specifically LAA. For instance, the mesh at the tip of the LAA is finer than at the centre of LA. Four boundary layers at wall boundaries were used to resolve the boundary layer flow (as shown in Figure 1). The total thickness was set to 0.85 of the tetrahedron side length. Pulmonary veins and the mitral valve were extended based on the PVs and the MV diameter in order to reduce boundary effects. These procedures were applied for all six variant meshes from the coarsest mesh to the finest.

The extracted surfaces were slightly smoothed out for computational fluid dynamics simulation by removing spikes and reducing noise by using MeshMixer (https://www.meshmixer.com). The meshes were generated by employing the Vascular Modeling ToolKit (www.vmtk.org).

Since patient-specific waveforms were not available for the cohort in grid convergence study, a generic pulsatile flow at pulmonary vein boundary condition as inlet. Since we are only interested in determining the required numerical resolution, we simulated two cardiac cycles to ensure that initial numerical transients are washed out from the first cycle. 5.5 L/min cardiac output based on a normal stroke volume and heart rate were applied. The cross-sectional area ratio between the pulmonary veins were employed to split and scale the generic LA inlet flow waveform boundary condition.

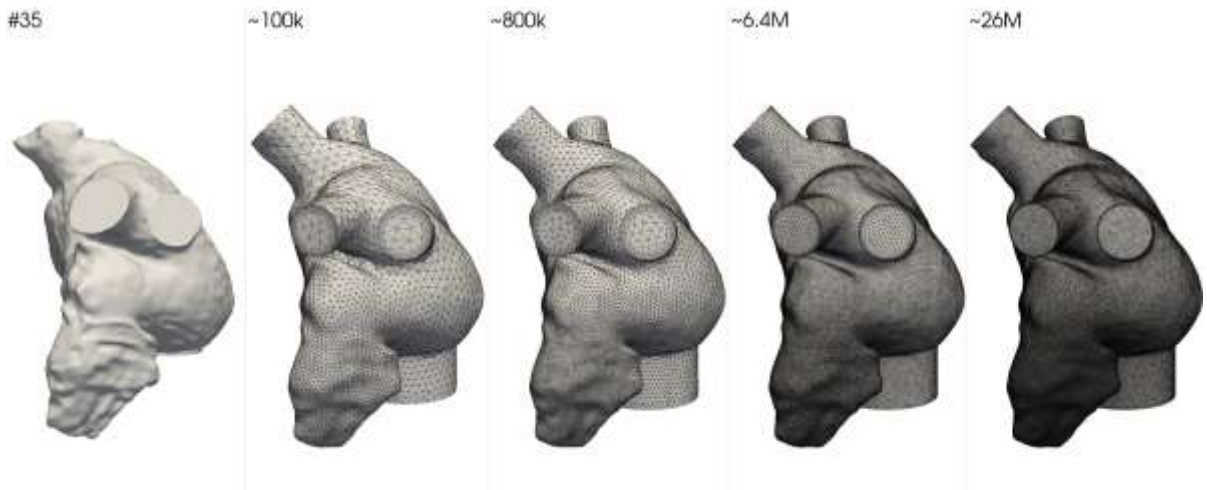

Figure 1. The leftmost shows the full lumen model before smoothing and generating mesh. Four different meshes coarse, medium and fine for case/geometry 35. Meshes with 400k and 3.2M are not presented.

2.3.1.3 Results

In the absence of an exact solution, the results for high-resolution mesh, i.e., 26 million tetrahedral elements, were chosen as reference values to compute the relative errors for TAWSS and OSI with different mesh resolutions. Cases 192, 26 and 4 were selected to present high, medium and low errors of convergence, respectively, in Figure 2. The exact values for the remaining cases are shown in the Appendix. Focusing first on quantitative results for TAWSS in the left atrium body, we can observe errors below 20% below 1 million tetrahedral elements. In contrast, there is a strong mesh dependency in the appendage with approximate errors up to 40% for the meshes below 7 million. For the three chosen cases, we can observe acceptable errors for meshes below 1 million and 7 million elements. However, for appendage, OSI is more sensitive which requires meshes up to 10 million elements to obtain the errors below 10%.

Shifting focus to qualitative results, Figure 3 shows isovelocity surfaces, TAWSS, OSI, RRT and ECAP for LA and LAA of those cases are quantitatively presented in Figure 2. The velocity field comparison shows that we can capture more instabilities of atrial flow with refined meshes up to 26M elements. For the coarse mesh with 100k elements, the flows are not smooth and reflective of a fluid flow, the flow patterns are difficult to interpret, and appear closer to numerical artefacts rather than dynamical behaviour of blood flow. Even with the meshes of 1M elements, the flows are not smooth enough to be visually acceptable. By employing finer meshes of 7M and 26M, the flows become smoother and more realistic patterns can be observed.

The corresponding TAWSS are shown in the next two rows. It can be seen that refining the mesh leads to different patterns of TAWSS with different high/low regions, caused by an evident increase of capturing the velocity and WSS instabilities. The different magnitudes in different regions are indicative of different dynamical flow behaviour, which were difficult to interpret from velocity results. Moreover, these effects are amplified in the LAA where thrombus can form. The latter suggests that the mesh resolution has a profound influence on the fundamental flow patterns in the LAA.

The third and fourth rows show the results of the OSI metric. OSI, as an indicator for flow oscillation in magnitude and direction, also shows high sensitivity to mesh resolutions. By refining the mesh, different OSI distributions that identify different high/low levels appeared. There are also significant differences in OSI distributions and levels in LAA. This is in agreement with our observation of velocity and WSS results.

RRT and ECAP are respectively presented in the last four rows. Although it is difficult to find a direct correlation between the qualitative and quantitative findings in RRT and ECAP, inspection of the results suggests that the qualitative differences in RRT and ECAP are still high in LA even though the quantitative convergence levels are achieved. Like previous results of TAWSS and OSI, RRT and ECAP show different patterns and high/low spots by employing high-resolution meshes. Moreover, more high levels of RRT and ECAP can be seen in LAA.

In conclusion, both qualitative and quantitative results show that mesh size selection has a noticeable effect on the prediction of intra-left atrial flow and hemodynamics. Therefore, it is critical to perform proper convergence studies to prove that a fluid simulation is independent of the mesh size.

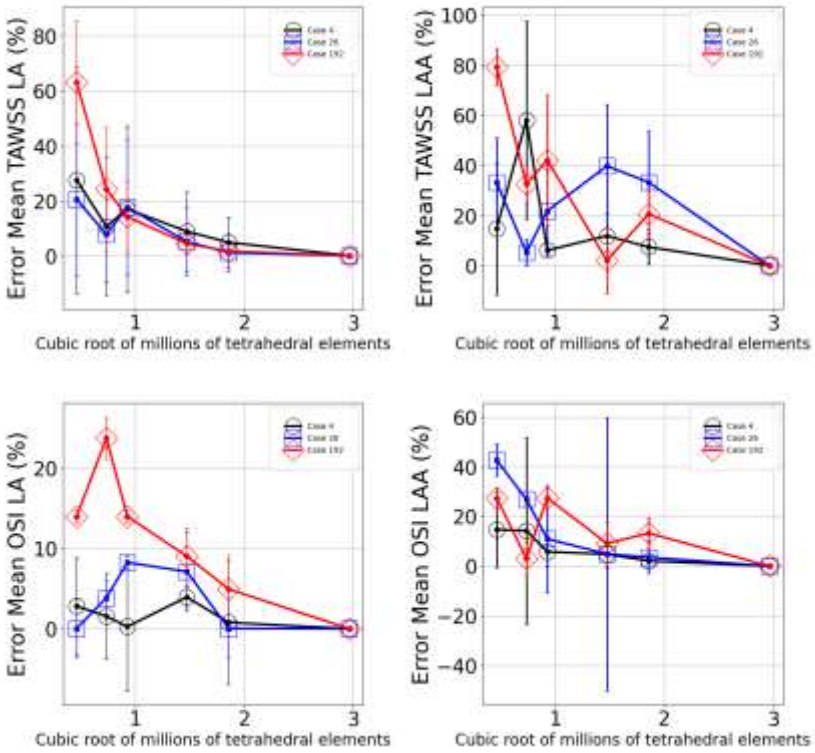

Figure 2 Quantitative differences in TAWSS and OSI for cases 192, 26 and 4. The relative error is computed.

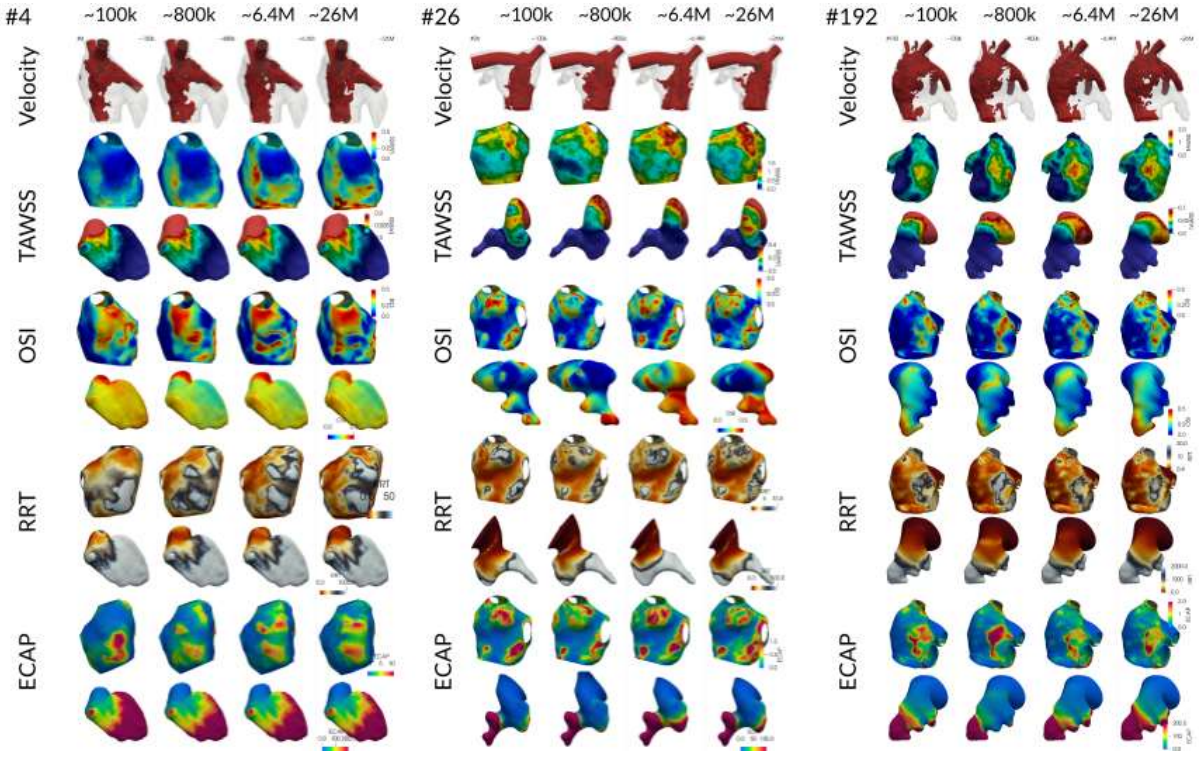

Figure 3. Qualitative impact of spatial resolution on cases 4, 26 and 192. For each case the first row compares isovelocity surfaces at the same time, the second and third rows compares TAWSS in LA and LAA, respectively, the fourth and fifth rows for OSI in LA and LAA, respectively, sixth and seventh rows RRT and eighth and ninth rows ECAP.

2.3.2 - Boundary layer sensitivity

The impact of boundary layers on resolving near-wall flow and predicting of hemodynamic indices were studied in this section. As can be seen from Figure 4, five different meshes were generated ranging from no boundary layers to eight layers, i.e. 0, 2, 4, 6, 8 boundary layers. The boundary layer thickness and sublayer ratio were kept constant for all meshes. The generated meshes are around 2.5 million tetrahedral elements in order to isolate the boundary layer effects as well as balance the computational cost and accuracy. The simulations were performed for an AF patient with patient-specific moving wall boundary condition. TAWSS, OSI, RRT and ECAP for all meshes are computed and shown qualitatively in Figure 5. The quantitative impact of the number of boundary layers are presented in Figure 6. It can be seen from qualitative and quantitative results that there are significant differences between no and 2 boundary layers against four and higher boundary layers. Highest errors have been observed for TAWSS and ECAP up to approximately 50%. The levels of convergence for the commonly reported hemodynamic indices will be reached for four, six and eight boundary layers. The results confirmed that four boundary layers along with 0.85 boundary layer thickness and 0.75 sub-layer ratio appeared to be an optimal choice for resolving blood flow near the wall.

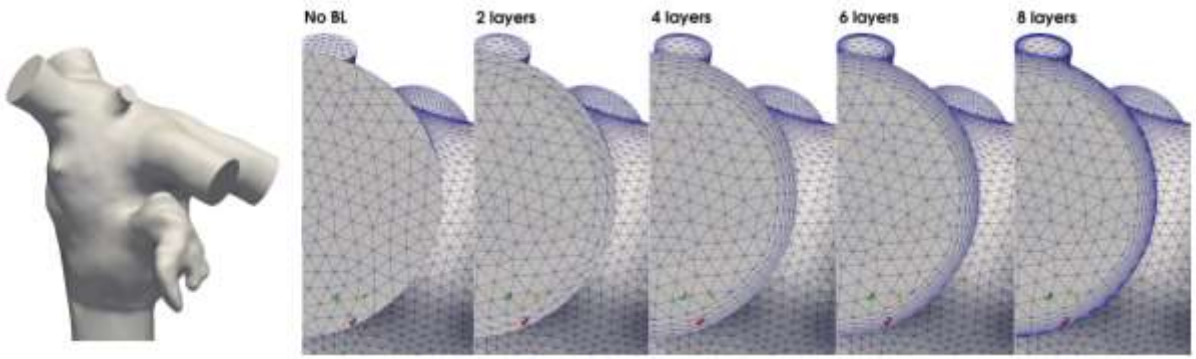

Figure 4. The leftmost is the geometry used for the study. The rest are the five different meshes employed with no boundary layers, 2, 4, 6 and 8 boundary layers.

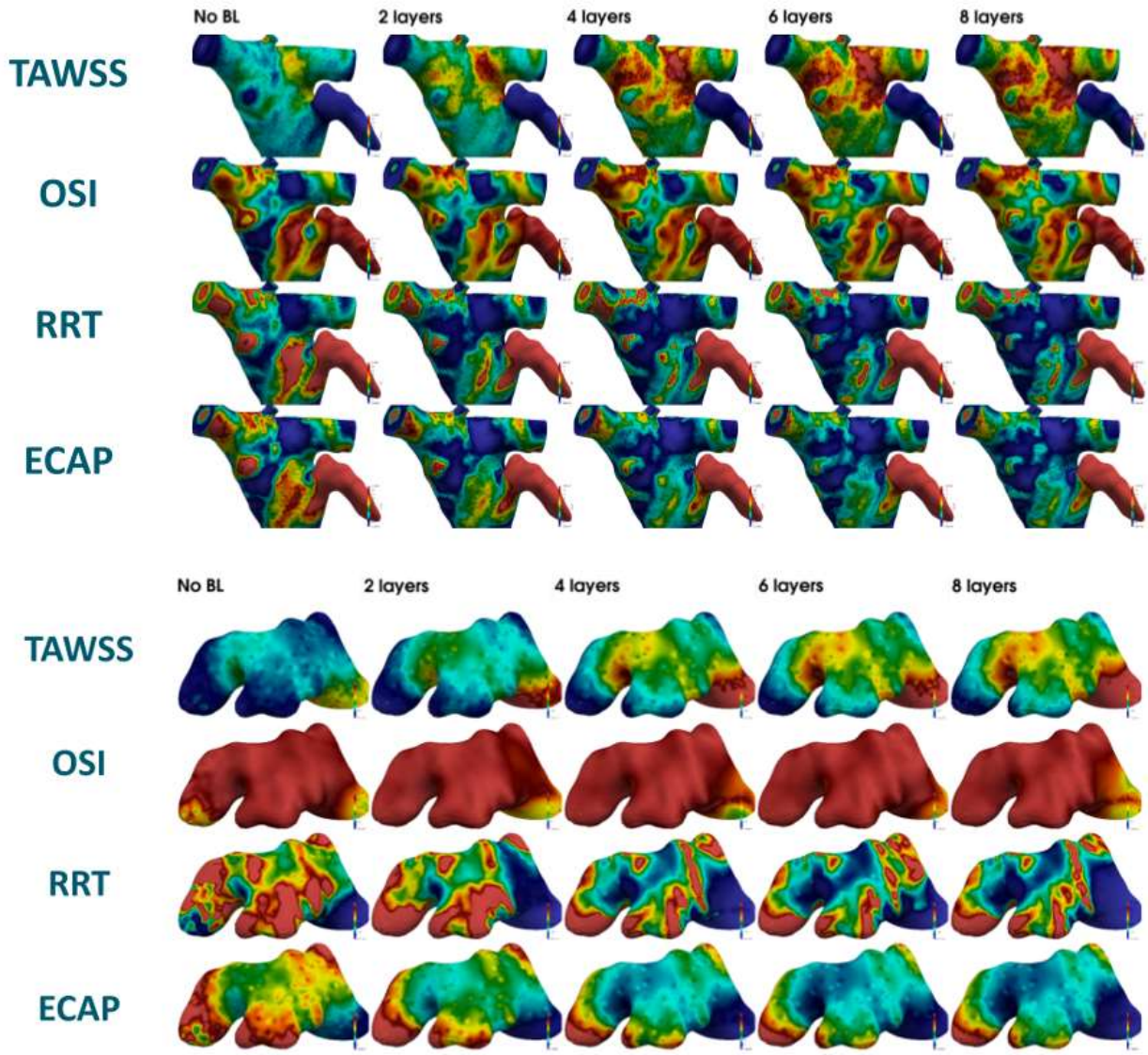

Figure 5. Qualitative impact of the number of boundary layers on hemodynamic indices. The first four rows show the results of TAWSS (scale: 0-2), OSI (scale: 0–0.5), RRT (scale: 0–20) and ECAP (scale: 0–10) in LA and LAA. The last four rows focus the results of TAWSS (scale: 0-0.2), OSI (scale: 0–0.5), RRT (scale: 0–500) and ECAP (scale: 0–15) on the LAA.

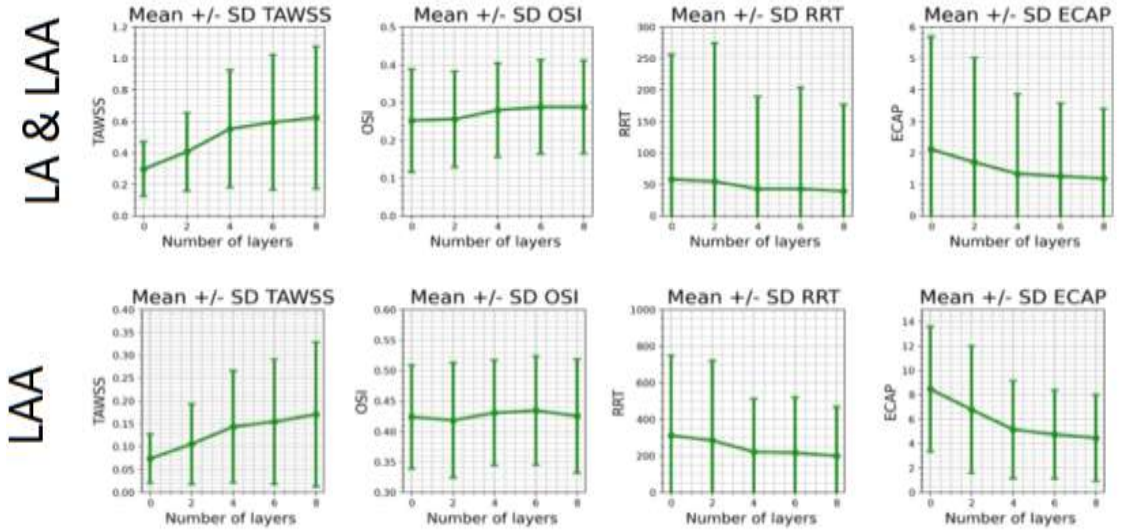

Figure 6. Quantitative impact of the number of boundary layers on considered hemodynamic indices in the left atria (LA) and left atrial appendage (LAA). The domain-averaged values plus/minus standard deviation are presented.

2.3.3 - Numerical solution strategy

The primary aim of this study is to investigate normal-resolution (NR) simulations in the context of the vast majority of published literature against high-resolution (HR) ones, with respect to numerical solution strategy. Recent studies of cerebral aneurysms have shown that the properties of the algorithm used to solve Navier-Stokes equations are as important as the temporal and spatial resolution to obtain accurate hemodynamic predictions (Valen-Sendstad & Steinman, 2013). To ensure the numerical experiment is as controlled as possible, simulations are performed by developing and validating solvers within the framework of open-source finite-element method library, FEniCS (http://fenicsproject.org/). For HR solver, overall second order accurate and minimally dissipative solver (https://github.com/mikaem/Oasis) which is open-source was employed and for NR solver, overall first order accurate which is commonly employed as default settings in commercial CFD solvers was used. The developed NR solver uses implicit backward Euler for discretization, with stabilisation schemes, such as streamline upwind Petrov-Galerkin (SUPG) in finite-elements (FEM) algorithms.

The vast majority of CFD-based atrial flow has reported using 100 to 1000-time steps per cardiac cycle with meshes of 100 thousand up to 2 million tetrahedral elements as presented in Table1. On the other hand, there are few studies in which 10000 or 20000 time-steps per cardiac cycle with meshes up to 17 million tetrahedral elements have been reported. To investigate the potential gap between normal-fidelity and high-fidelity approaches to predict the flow physics of the left atrium, NR and HR simulations were compared. NR simulations were performed by employing 1000 time-steps per cardiac cycle with meshes of 1 million tetrahedral elements as well as NR solver in which typically are used in the vast majority of the literature and compared against HR simulations where 10000 time-steps per cardiac cycle with meshes of 26 million elements and HR solver used for simulations.

The solution fidelity was qualitatively evaluated via isovelocity surfaces and maps of domain-averaged TAWSS, OSI, RRT and ECAP. Qualitative results for four cases are summarised in the comprehensive way in Figure 7. All NR simulations showed smoothed and laminar flows in contrast to the HR simulations which showed highly unstable and turbulent flows. HR simulations show different TAWSS and OSI patterns with different high/low regions compared to the corresponding NR ones. On the contrary, RRT and ECAP are surprisingly robust and show relatively less sensitivity to the numerical strategies. The quantitative impact on considered hemodynamic indices is shown in Figure 8. As can be seen from Figure 9, quantitative results of domain -averaged TAWSS and OSI for NR simulations unpredict TAWSS and OSI compared to NR which is alignment with qualitative results. This can be interpreted as NR numerical strategy suppressing artificially all flow instabilities. The highest relative errors between HR and NR strategies for TAWSS and OSI have been found 21% and 29% in case 26 and case 4, respectively. Domain-averaged RRT and ECAP shows relatively less affected except for cases 26 and 167 in which 60% errors appeared.

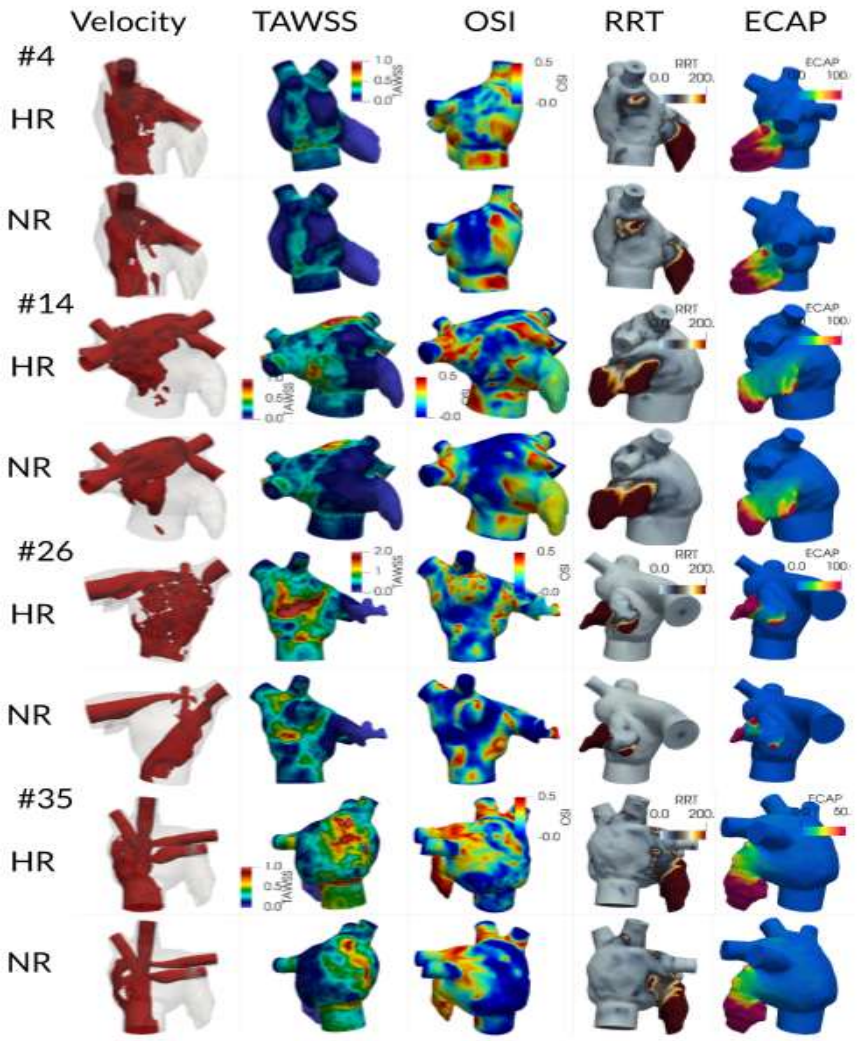

Figure 7. Qualitative impact of solution fidelity on velocity, TAWSS, OSI, RRT and ECAP distributions. For each of the cases, the first column shows isosurfaces of peak diastolic velocity magnitude, the second column shows time-averaged WSS magnitude (scale: 0–1 or 2), and the third column shows the OSI (scale: 0.0–0.5), the fourth column shows RRT (scale: 0-200) and the fifth column shows ECAP (scale: 0-100).

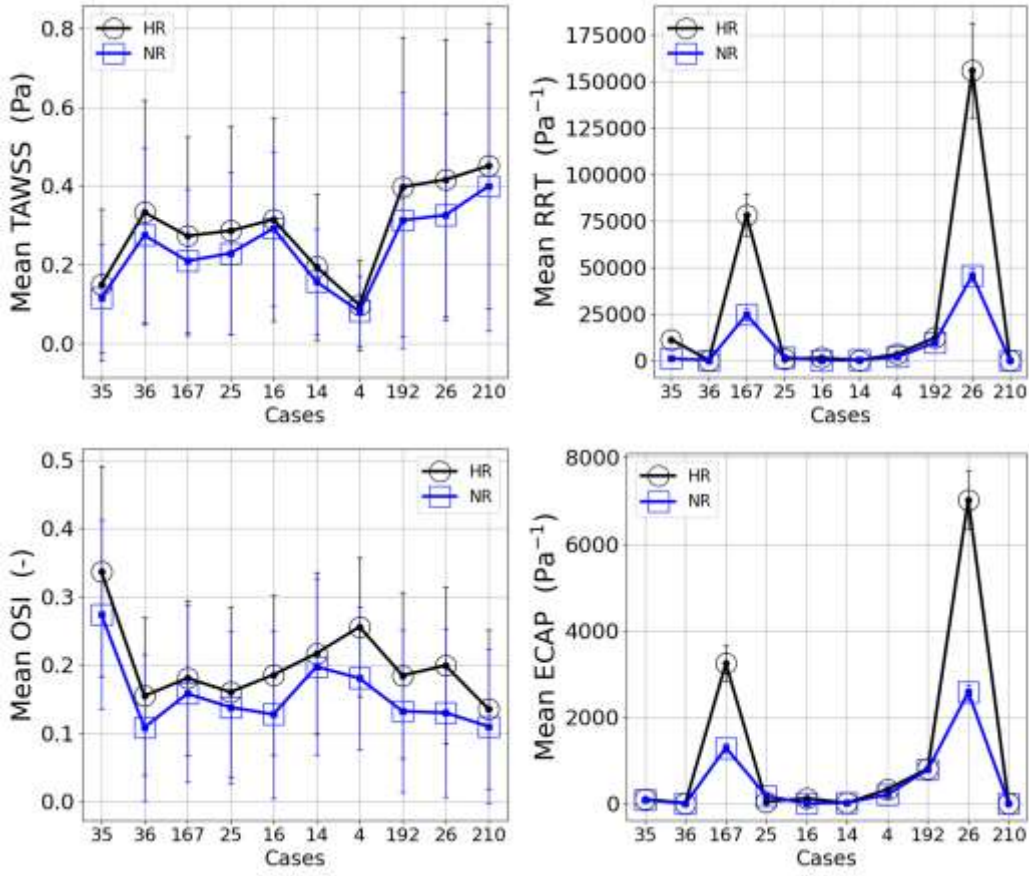

Figure 8. The quantitative impact of solution fidelity on considered hemodynamic indices for different cases. The domain-averaged values plus/minus standard deviations of LA and LAA are plotted.

2.3.4 - Boundary conditions

2.3.4.1 Methodology

A dataset of six patients from Hospital de la Santa Creu i Sant Pau (Barcelona), who underwent a LAAO, were selected for the study. The selection was based on the availability of a complete CT study at follow-up including the whole atrium anatomy and an echocardiography (transesophageal, TTE) study with mitral flow analysis. All patients had non-valvular atrial fibrillation. One of them (Pat2) also presented severe mitral regurgitation. Three patients (Pat4-6) had a history of DRT after LAAO with the Amulet device (Abbott Vascular, Santa Clara, CA, USA). The study protocol was approved by the local ethical committee of the hospital, and patient written consents were obtained. CT images were acquired at least twice, between months 1-3 and months 3-6 after LAAO implantation, respectively. This dataset is also used in the study of section 3.3.5.

2.3.4.2 Inlet/outlet and wall behaviour scenarios

Because of the large variability of boundary conditions found in the literature for LA fluid modelling, the influence of the most common corresponding approximations on the simulation results was evaluated. In particular, different configurations of inlets and outlets at the pulmonary veins (PVs)

and mitral valve (MV) were tested, respectively. Fluid pressure or velocity profiles at the PV (inlet) and MV (outlet) were selected either from the literature or from patient-specific data. Furthermore, the impact of dynamic behaviour of the LA wall was compared to the classical assumption of rigid walls (Mill et al., 2021).

Four different scenarios of boundary conditions were tested to identify the numerical approximations that lead to the most reliable DRT in silico predictions after LAAO device implantation.

2.3.4.2.1 Scenario 1: constant (null) inlet pressure, imaging-based outlet velocities and rigid wall

The first scenario consisted of setting up a constant inlet pressure equal to 0 mmHg, as in (Bosi et al., 2018, Dillon-Murphy et al., 2018), while a patient-specific Doppler-based velocity profile was defined in the MV outlet. Mitral velocities from Doppler data were quite variable for different patients, from 0.4 to 3 m/s. The LA wall was considered rigid, i.e., without movement, resulting in a pure Computational Fluid Dynamics (CFD) modelling study. Such an assumption is a common approach in the literature (Dillon-Murphy et al., 2018, Bosi et al., 2018, García-Isla et al., 2018, Aguado et al., 2019, Aguado et al., 2019, Wang et al., 2020, Sanatkhani et al., 2021), which is based on the reduced wall movement in patients with atrial fibrillation.

Scenario 1 resulted in pressure values from -100 Pa (-0.75 mmHg) to 300 Pa (2.25 mmHg), which were substantially lower than the ones measured with invasive catheters, which ranged from 6 mmHg to 12 mmHg. In addition, the simulated mean pressure gradient between the PV and MV was 190 Pa (1.43 mmHg), being much higher than those acquired in the clinical set-up (between 0.07 and 0.5 mmHg). Velocity magnitudes were within the physiological range, with blood flow patterns (see Figure 9) qualitatively simpler than in other scenarios, without obvious re-circulations despite the clinical evidence of DRT. Pressure values were homogeneous in the whole LA. The highest values of ECAP (i.e. linked to higher thrombogenic risk) were obtained at the LAAO device's surface, at the upper part, near the pulmonary ridge.

2.3.4.2.2 Scenario 2: patient pressure wave as inlet, imaging-based outlet velocities and rigid wall

The second scenario replaced the constant inlet pressure in Scenario 1 to the available pressure waves in the pulmonary veins of an AF patient. For each simulated case, this AF pressure wave was personalised, as it was adapted to the cardiac rhythm of each patient, derived from the ECG. A smoothing filter was also applied to the pressure wave to remove the noise in the signal. Similar to Scenario 1, patient-specific velocities were set up as outlet boundary conditions and the LA wall was assumed as rigid.

The inclusion of a AF patient pressure wave at the inlet BCs in Scenario 2 (i.e. pressure wave from AF patient at the inlet pulmonary veins, velocity curve from a generic ultrasound images as mitral valve outlet, with rigid wall behaviour) provided a more realistic simulated pressure map than in Scenario 1, as illustrated in Figure 9. Pressure values ranged from 125 Pa (0.94 mmHg) to 1110 Pa (8.33 mmHg), while the mean PV-MV gradient was of 15 Pa (0.11 mmHg), which were closer to clinical measurements than in Scenario 1. Velocity streamlines showed more re-circulations with low velocities (blue-green in Figure 9) near the device than in Scenario 1. Regions of high ECAP were similarly located as in Scenario 1, but with slightly higher values.

2.3.4.2.3 Scenario 3: patient pressure wave as inlet, imaging-based outlet velocities and dynamic mesh wall deformation

Scenario 3 takes in the deformation of the LA wall to study the differences in comparison with the rigid wall assumption in the previous scenarios. In the literature, some studies imposed LA deformation extracted from the processing of CT or MR images into the fluid simulations (Otani et al., 2016, Dillon-Murphy et al., 2018, Masci et al., 2019, García-Villalba et al., 2020), while others developed advanced fluid-structure interaction models (Zhang & Gay, 2008, Fang et al., 2021). When dynamic medical images are not available, an interesting alternative is to use a dynamic mesh approach (Mill et al., 2020, D'Alessandro et al., 2020, D'Alessandro et al., 2020) with displacements generated either synthetically or from literature data.

In this scenario, a dynamic mesh approach was applied to the LA meshes in which the displacements of the LA results from the Laplace equation. The dynamic mesh algorithm to simulate the displacement of the MV annulus ring was applied based on a function described in the work of Veronesi et al., 2008. Patients with non-valvular AF usually present similar longitudinal MV annulus ring movement as the healthy ones (i.e. from 8 to 10 mm) (Emilsson & Wandt, 2000). The resulting dynamic mesh displacements were also synchronised to each patient, based on the cardiac rhythm extracted from each individual ECG and using linear interpolation functions.

The inclusion of a dynamic mesh-based movement in Scenario 3 led to lower pressure values near the device's surface compared to Scenario 2. Pressure values ranged from 174 Pa (1.31 mmHg) to 1240 (9.30 mmHg), with the average PV-MV pressure gradient of 11 Pa (0.08 mmHg). The blood flow patterns in Scenario 3 (see Figure 9) showed more re-circulations than the other scenarios, with complex haemodynamic areas near the LAAO device, including low velocities. Interestingly, the ECAP map of Scenario 3 presented a new area with high risk of thrombus formation, at the right side of the device, in addition to the area identified in previous scenarios.

2.3.4.2.4 Scenario 4: literature velocity profile as inlet, mitral valve as wall (systole) or constant pressure (diastole) and dynamic mesh wall deformation

The fourth studied scenario represented a different set of boundary conditions, often found in the literature (Zhang & Gay, 2008, Zhang & Gay, 2008, Aguado et al., 2019, Jia et al., 2019, Qureshi et al., 2020, Qureshi et al., 2020, Sanatkhani et al., 2021). A velocity profile was imposed in the PV inlets, while the mitral valve is modelled as a wall during ventricular systole and with a constant pressure at diastole (equal to 8 mmHg in our study). A generic PV velocity profile from literature was used in all analysed cases since it was not possible to obtain reliable PV velocity curves from all the available echocardiographic studies (i.e., insufficient visual window in some locations such as the right superior pulmonary vein). The LA wall behaviour was modelled with the dynamic mesh approach, as in Scenario 3.

Fluid simulations with Scenario 4 boundary conditions diverged in four out of the six analysed cases, whereas convergence was reached for all cases in the rest of the scenarios. With its opposite BC strategy (i.e. velocities at inlets and pressures at outlets), Scenario 4 provided substantially different haemodynamic in-silico indices compared to the other three scenarios. Pressure maps provided during ventricular systole (i.e. MV closed without outlet pressure BC) were similar to Scenario 1 (around 0 Pa). With the opening of the mitral valve in ventricular diastole and the application of constant outlet pressure BC, the pressure raised up to 1200 Pa (9 mmHg), resulting in the largest pressure range in all scenarios. In contrast, the pressure gradient between the PV and MV was 4 Pa (0.03 mmHg), i.e. the lowest in any of the tested boundary conditions. High blood velocities were

found in the superior part of the LA, in contrast to other scenarios. However, blood flow stagnation was also largely pronounced in the inferior part of the LA, presenting very low velocities (blue streamlines in Figure 9). The consequence of this flow over-stagnation was an ECAP mapping with high values almost all over the LA, making it difficult to distinguish thrombogenic from healthy areas.

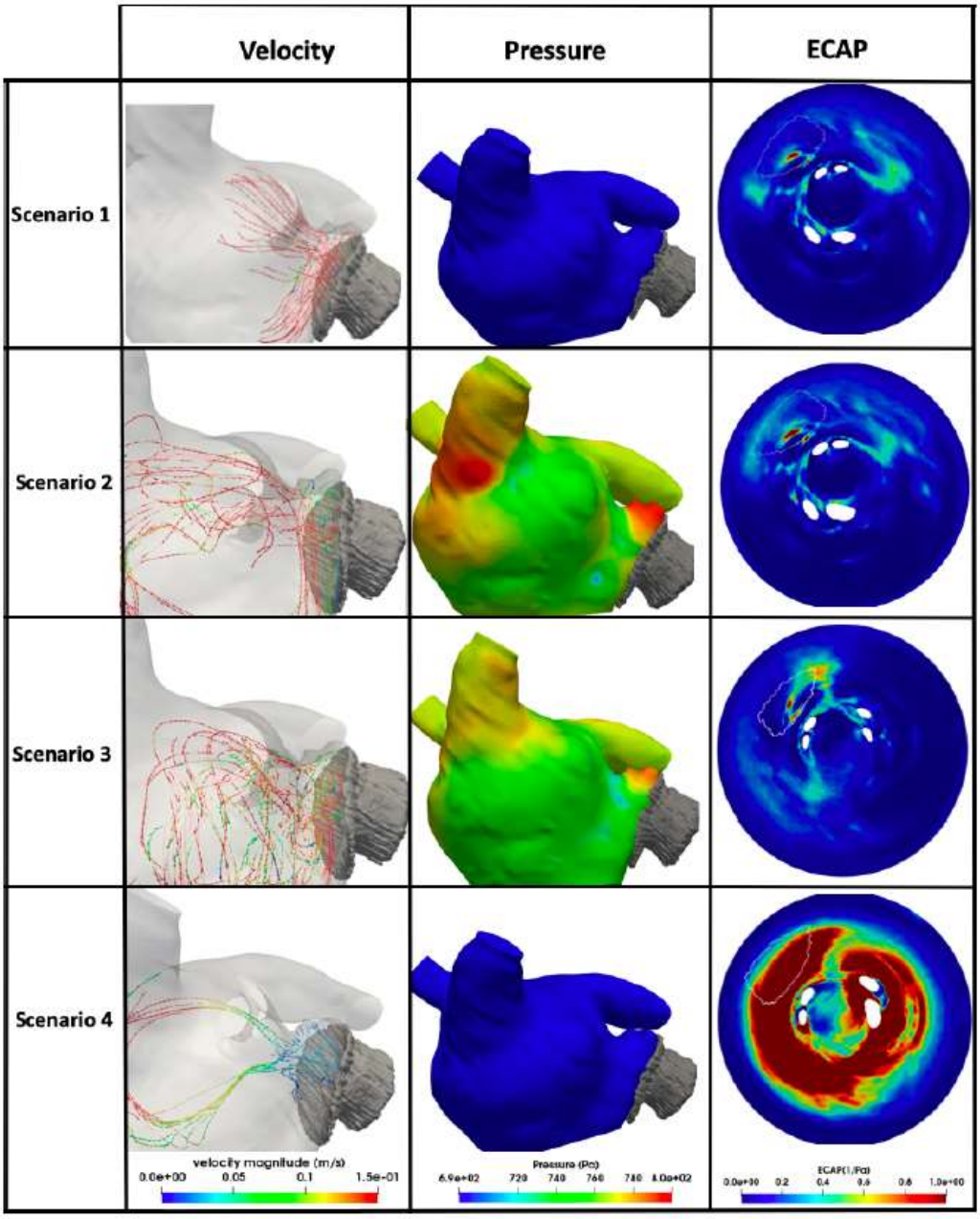

Figure 9. Haemodynamic in-silico indices obtained with different boundary condition scenarios (1-4). ECAP: endothelial cell activation potential. The white line in the ECAP maps indicate the position of the implanted device. Scenario 1: null inlet pressure, imaging-based outlet velocities and rigid wall, Scenario 2: as Scenario 1 but with patient pressure wave as inlet; Scenario 3: as Scenario 2 but with dynamic mesh wall deformation; Scenario 4: literature velocity profile as inlet, mitral valve as wall (systole) or constant pressure (diastole) and dynamic mesh wall deformation (Mill et al., 2021).

2.3.5 - Device-related thrombus (DRT)

In-silico fluid simulations have the potential to play a major role in the optimisation of LAAO procedures, contributing to better understanding of haemodynamics after the implantation in order to avoid adverse outcomes such as the formation of DRT. Among the evaluated boundary conditions (in Section 3.3.4), scenarios that converged (all except Scenario 4) found lower blood flow velocities next to the LAAO device's surface in DRT cases, below the threshold (0.20 m/s) reported for thrombosis risk (García-Fernández et al., 1992). However, ECAP and RRT maps from Scenario 3 (generic AF pressure wave as PV inlet, echocardiography-based velocity profile as MV outlet and dynamic mesh LA wall behaviour) were the most accurate to assess DRT risk and predict the possible localisation of the formed thrombus. Figure 11 clearly shows elevated ECAP and RTT values around the implanted LAAO device in DRT cases compared to non-DRT ones, which can also be observed in Figure 12, qualitatively analysing blood flow re-circulations and lower velocities in these areas. For instance, in-silico haemodynamic indices for Pat6 perfectly predicted DRT in the superior-anterior part of the LAAO device. Nevertheless, ECAP maps might not be specific enough to identify the exact location of DRT in cases where the pulmonary ridge (space between the LAA and the LSPV) is not covered (see Pat4 and Pat5 in Figure 12). Furthermore, it is not obvious to define a consistent threshold in the ECAP and RRT maps to determine the risk of DRT for all cases. In the studied cases, ECAP values larger than 0.5 Pat1 were associated with DRT areas but we could not find a conclusive threshold for RRT, which should be computed in more than two cardiac cycles. Despite the mentioned limitations of ECAP and RRT indices, they were good descriptors of the overall LA haemodynamics that combined with velocity magnitudes and blood flow recirculation analysis can be used to assess the risk of DRT after LAAO implantation.

Figure 10 shows the mean blood flow velocities near the surface of the implanted LAAO device in all analysed cases, including simulations with different boundary conditions scenarios. It can easily be observed that DRT cases (Pat4-6) had lower velocities (< 0.20 m/s) than patients without thrombogenic history (Pat1-3), independently of the BC scenarios. Interestingly, the second case (Pat2), which suffered from a several mitral regurgitation (MR), presented substantially higher velocities than the remaining cases

Two-dimensional flattened maps of the LA showing the distribution of the ECAP and RRT in-silico haemodynamic indices in the six studied cases (with Scenario 3 boundary conditions) can be seen in Figure 11. Similarly to the analysis of the blood flow velocities near the device surface, DRT and non-DRT cases present substantial differences in ECAP and RRT, with the former showing larger values, especially in the device surroundings. Both ECAP and RRT maps depicted comparable distribution maps, with RRT showing more areas with maximum values. Figure 11 shows the follow-up CT scans of all analysed patients together with the simulated blood flow patterns, including where the thrombus was formed in DRT cases. It can be observed a good agreement between thrombus localisation and areas with low blood flow velocities and complex patterns (i.e., re-circulations) in the fluid simulations.

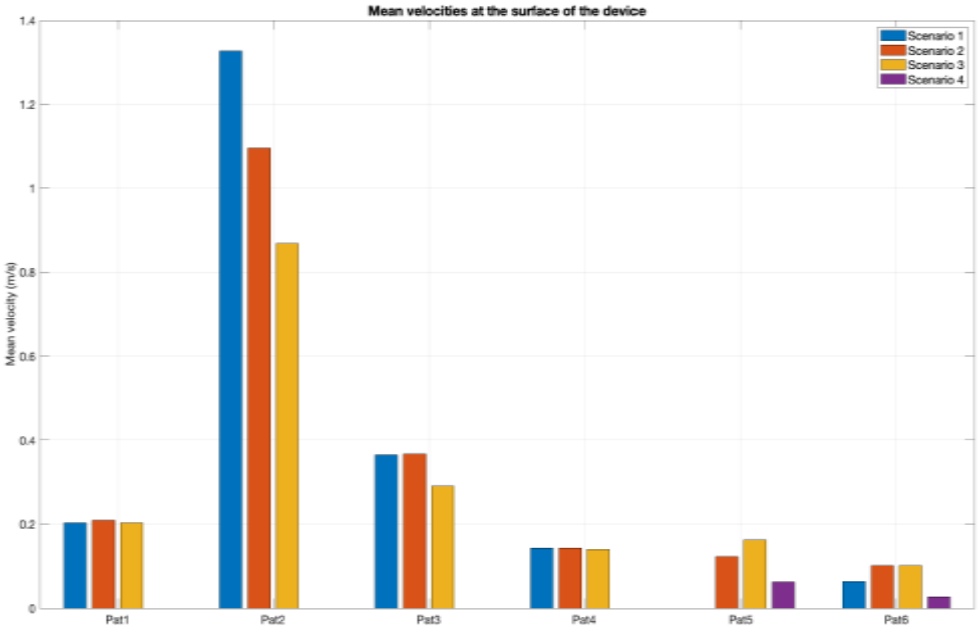

Figure 10. Average blood flow velocities near the device surface for the different simulated scenarios in all analysed patients. Pat1-3 and Pat4-6 were without and with device-related thrombus, respectively.

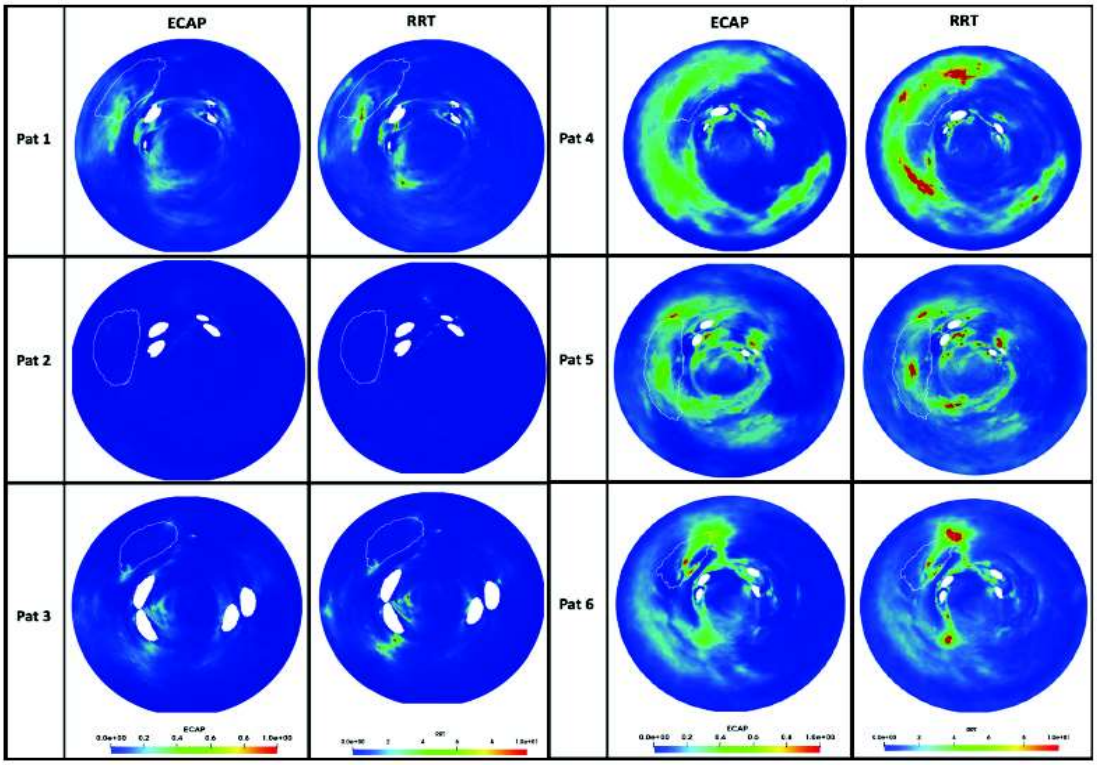

Figure 11. In-silico haemodynamic indices for the prediction of device-related thrombosis (DRT) after left atrial appendage occlusion in the six analysed cases: Pat1-3 were controls and Pat4-6 had DRT. Higher values (red colour) indicate a higher risk of thrombosis. The white line in the 2D maps signals the position of the implanted device. ECAP: endothelial cell activation potential; RRT: relative residence times.

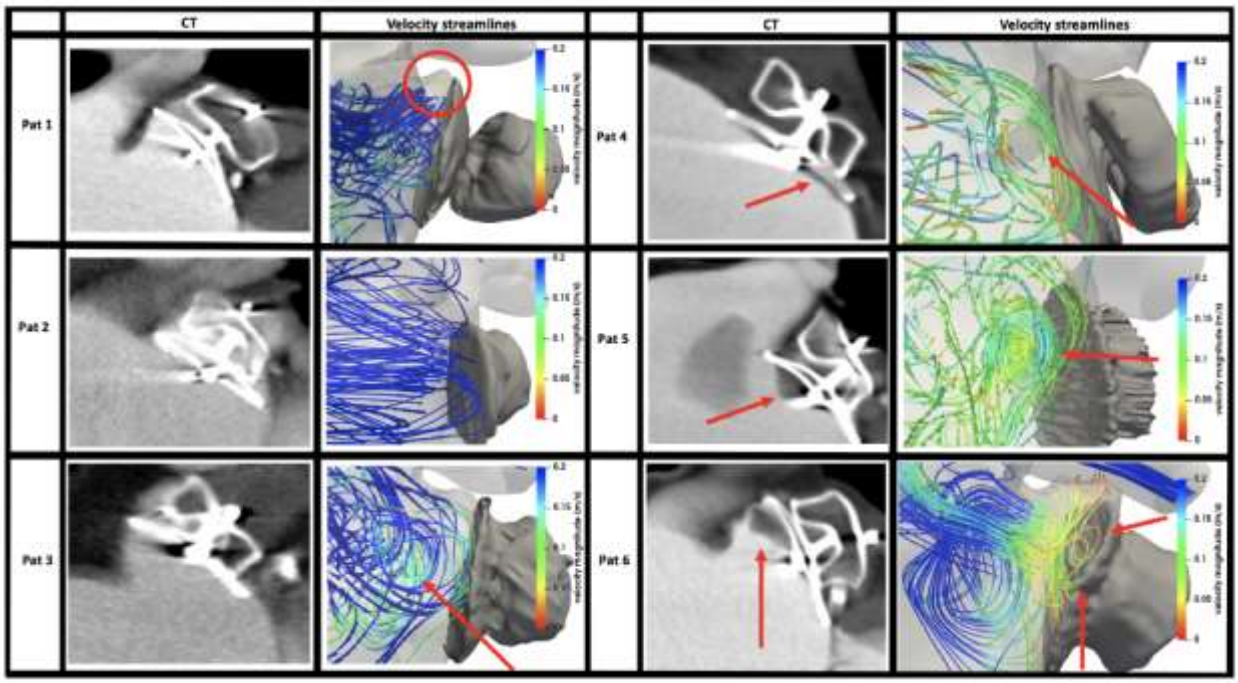

Figure 12. Computed Tomography (CT) scans after left atrial appendage implantation for cases with (Pat4-6) and without (Pat1-3) device-related thrombus together with streamline-based visualisation of the simulate blood flow patterns, coloured by velocity magnitude (blue and red corresponding to high and low values, respectively). Red arrows in CT scans indicate where the thrombus was found.

3 - Discussion

In this work we have presented a sensitivity analysis to demonstrate the relevance of the most important modelling choices in LA fluid modelling for the prediction of blood flow physics and DRT after LAAO implantation by using patient-specific geometries from CT scans. The obtained results in Section 3 confirmed that the modelling choices and boundary conditions are critical for predicting hemodynamic indices and subsequently thrombus formation.

The question of when a mesh is suitable enough to predict accurate flow physics and hemodynamic indices depends on many factors, including uncertainties of the input data such as patient image resolution/segmentation and flow rates, the quality of implemented boundary conditions, the robustness of the flow solver and numerical schemes and, importantly, the needs of the analyst. In the absence of a comprehensive correlation of these factors, fluid simulation could basically lead to providing unrealistic blood flow patterns and predictions. That being said, we have assumed in the current study that the blood flow has Newtonian rheology which can be considered as a limitation for the study. Currently, We are investigating the effect of non-Newtonian rheology for blood flow simulation in the left atrium which will be presented in the near future.

Our study spanned a wider range of meshes compared to literature, with high-resolution meshes comprising 26 million elements to coarse meshes with 100 thousand elements and allowed investigation of the isolated effects of boundary layers. Furthermore, we studied different temporal resolutions from 10 ms to 0.1 ms in the context of the solution strategy and accuracy of numerical solvers. Our present findings suggest that high spatial and temporal resolutions along with a minimally dissipative, second-order-accurate CFD solver are sufficient to resolve the dynamics of

atrial flows. The flow modelling options have a pronounced effect on the prediction of hemodynamic indices in the left atrium, approximately the same as uncertainties like flow rates.

The recommended approach for boundary conditions is to leverage as much patient-specific data as possible to personalise the fluid models, especially velocity/pressure waveforms at the PV/MV and LA wall deformation, from medical images such as echocardiography and dynamic CT/MR scans, ensuring a good match between blood flow (velocities), LA volume changes and wall deformation. Despite being difficult to obtain all the required data for every case, it should be sufficient to acquire either velocity profiles (easier at the MV for outlet BC) or LA wall movement, and set up the remaining boundary conditions accordingly (Mill et al., 2021).

4 - Conclusions

In this study, we have presented a sensitivity analysis of different computational fluid dynamics options and boundary conditions scenarios available in the literature to identify the optimal modelling choices for predicting hemodynamic indices and subsequently thrombus formation particularly DRT.

The results signify that it is therefore essential that analysts carry out proper verification studies, per the recommendations of technical computational experts in theory and practice, to reach solver settings, spatial and temporal resolutions that can uncritically be applied to any given case.

Moreover, the obtained results for different scenarios of boundary conditions demonstrated the need for assimilating into the models patient-specific data from medical images, such as MV velocities from echocardiography, to synchronise LA anatomy, wall deformation and pressure/velocity profiles at the inlets/outlet. Moreover, the use of generic pressure waves (rather than constant values) and dynamic LA walls achieved more physiological simulation results.

5 - References

Aguado, A. M., Olivares, A. L., Yagüe, C., Silva, E., Nuñez-García, M., Fernandez-Quilez, Á., Mill, J., Genua, I., Arzamendi, D., De Potter, T., Freixa, X., & Camara, O. (2019). In silico Optimization of Left Atrial Appendage Occluder Implantation Using Interactive and Modeling Tools. *Frontiers in Physiology*, *10*(35). https://doi.org/10.3389/fphys.2019.00237

Aronow, W. S., & Banach, M. (2009). Atrial fibrillation: The new epidemic of the ageing world. *Journal of Atrial Fibrillation*, *1*(6). https://doi.org/10.4022/jafib.v1i6.530

Bosi, G. M., Cook, A., Rai, R., Menezes, L. J., Schievano, S., Torii, R., & Burriesci, G., Burriesci. (2018). Computational fluid dynamic analysis of the left atrial appendage to predict thrombosis risk. *Frontiers in Cardiovascular Medicine*, *5*(1). https://doi.org/10.3389/fcvm.2018.00034

Cresti, A., García-Fernández, M. A., Sievert, H., Mazzone, P., Baratta, P., Solari, M., Geyer, A., De Sensi, F., & Limbruno, U. (2019). Prevalence of extra-appendage thrombosis in non-valvular atrial fibrillation and atrial flutter in patients undergoing cardioversion: A large transoesophageal echo study. *EuroIntervention*, *15*(3), e225–e230. https://doi.org/10.4244/eij-d-19-00128

Dahl, S. K., Thomassen, E., Hellevik, L. R., & Skallerud, B. (2012). Impact of pulmonary venous locations on the intra-atrial flow and the mitral valve plane velocity profile. *Cardiovascular Engineering and*

Technology, *3*(3), 269–281. https://doi.org/10.1007/s13239-012-0099-1

D'Alessandro, N., Masci, A., Andalò, A., Dedè, L., Tomasi, C., Quarteroni, A., & Corsi, C. (2020, December 30). Simulation of the hemodynamic effects of the left atrial appendage occlusion in atrial fibrillation: Preliminary results. *2020 Computing in Cardiology Conference (CinC)*. http://dx.doi.org/10.22489/cinc.2020.302

Dillon-Murphy, D., Marlevi, D., Ruijsink, B., Qureshi, A., Chubb, H., Kerfoot, E., O'Neill, M., Nordsletten, D., Aslanidi, O., & de Vecchi, A. (2018). Modeling left atrial flow, energy, blood heating distribution in response to catheter ablation therapy. *Frontiers in Physiology*, *9*. https://doi.org/10.3389/fphys.2018.01757

Dueñas-Pamplona, J., García, J. G., Sierra-Pallares, J., Ferrera, C., Agujetas, R., & López-Mínguez, J. R. (2021a). A comprehensive comparison of various patient-specific CFD models of the left atrium for atrial fibrillation patients. *Computers in Biology and Medicine*, *133*, 104423. https://doi.org/10.1016/j.compbiomed.2021.104423

Dueñas-Pamplona, J., García, J. G., Sierra-Pallares, J., Ferrera, C., Agujetas, R., & López-Mínguez, J. R. (2021b). A comprehensive comparison of various patient-specific CFD models of the left atrium for atrial fibrillation patients. *Computers in Biology and Medicine*, *133*(1), 104423. https://doi.org/10.1016/j.compbiomed.2021.104423

Emilsson, & Wandt. (2000). The relation between ejection fraction and mitral annulus motion before and after direct-current electrical cardioversion. *Clinical Physiology*, *20*(3), 218–224. https://doi.org/10.1046/j.1365-2281.2000.00249.x

Fang, R., Li, Y., Zhang, Y., Chen, Q., Liu, Q., & Li, Z. (2021). Impact of left atrial appendage location on risk of thrombus formation in patients with atrial fibrillation. *Biomechanics and Modeling in Mechanobiology*, *1*(1). https://doi.org/10.1007/s10237-021-01454-4

Feng, L., Gao, H., Griffith, B., Niederer, S., & Luo, X. (2019). Analysis of a coupled fluid-structure interaction model of the left atrium and mitral valve. *International Journal for Numerical Methods in Biomedical Engineering*, *35*(11). https://doi.org/10.1002/cnm.3254

García-Fernández, M. A., Torrecilla, E. G., Román, D. S., Azevedo, J., Bueno, H., Moreno, M. M., & Delcán, J. L. (1992). Left atrial appendage doppler flow patterns: Implications on thrombus formation. *American Heart Journal*, *124*(4), 955–961. https://doi.org/10.1016/0002-8703(92)90978-5

García-Isla, G., Olivares, A. L., Silva, E., Nuñez-Garcia, M., Butakoff, C., Sanchez-Quintana, D., G. Morales, H., Freixa, X., Noailly, J., De Potter, T., & Camara, O. (2018). Sensitivity analysis of geometrical parameters to study haemodynamics and thrombus formation in the left atrial appendage. *International Journal for Numerical Methods in Biomedical Engineering*, *34*(8), e3100. https://doi.org/10.1002/cnm.3100

García-Villalba, M., Rossini, L., Gonzalo, A., Vigneault, D., Martinez-Legazpi, P., Flores, O., Bermejo, J., McVeigh, E., Kahn, A. M., & del Álamo, J. C. (2020). *Demonstration of patient-specific simulations to assess left atrial appendage thrombogenesis risk*. Cold Spring Harbor Laboratory. http://dx.doi.org/10.1101/2020.05.07.083220

Hur, J., Kim, Y. J., Lee, H.-J., Nam, J. E., Ha, J.-W., Heo, J. H., Chang, H.-J., Kim, H. S., Hong, Y. J., Kim, H. Y., Choe, K. O., & Choi, B. W. (2011). Dual-Enhanced cardiac CT for detection of left atrial appendage thrombus in patients with stroke. *Stroke*, *42*(9), 2471–2477. https://doi.org/10.1161/strokeaha.110.611293

Jia, D., Jeon, B., Park, H.-B., Chang, H.-J., & Zhang, L. T. (2019). Image-Based flow simulations of pre- and post-left atrial appendage closure in the left atrium. *Cardiovascular Engineering and Technology*, *10*(2), 225–241. https://doi.org/10.1007/s13239-019-00412-7

Koizumi, R., Funamoto, K., Hayase, T., Kanke, Y., Shibata, M., Shiraishi, Y., & Yambe, T. (2015). Numerical analysis of hemodynamic changes in the left atrium due to atrial fibrillation. *Journal of Biomechanics*, *48*(3), 472–478. https://doi.org/10.1016/j.jbiomech.2014.12.025

Marsden, A. L. (2014). Optimization in cardiovascular modeling. *Annual Review of Fluid Mechanics*, *46*(1), 519–546. https://doi.org/10.1146/annurev-fluid-010313-141341

Masci, A., Barone, L., Dedè, L., Fedele, M., Tomasi, C., Quarteroni, A., & Corsi, C. (2019). The impact of left atrium appendage morphology on stroke risk assessment in atrial fibrillation: A computational fluid dynamics study. *Frontiers in Physiology*, *9*(1). https://doi.org/10.3389/fphys.2018.01938

Mill, J., Agudelo, V., Olivares, A. L., Pons, M. I., Silva, E., Nuñez-Garcia, M., Morales, X., Arzamendi, D., Freixa, X., Noailly, J., & Camara, O. (2021). Sensitivity analysis of in silico fluid simulations to predict thrombus formation after left atrial appendage occlusion. *Mathematics*, *9*(18), 2304. https://doi.org/10.3390/math9182304

Mill, J., Harrison, J., Legghe, B., Olivares, A. L., Morales, X., Noailly, J., Iriart, X., Cochet, H., Sermesant, M., & Camara, O. (2021). In-Silico analysis of the influence of pulmonary vein configuration on left atrial haemodynamics and thrombus formation in a large cohort. In *Functional Imaging and Modeling of the Heart* (pp. 605–616). Springer International Publishing. http://dx.doi.org/10.1007/978-3-030-78710-3_58

Mill, J., Olivares, A. L., Arzamendi, D., Agudelo, V., Regueiro, A., Camara, O., & Freixa, X. (2020). Impact of flow dynamics on device-related thrombosis after left atrial appendage occlusion. *Canadian Journal of Cardiology*, *36*(6), 968.e13-968.e14. https://doi.org/10.1016/j.cjca.2019.12.036

Otani, T., Al-Issa, A., Pourmorteza, A., McVeigh, E. R., Wada, S., & Ashikaga, H. (2016a). A computational framework for personalized blood flow analysis in the human left atrium. *Annals of Biomedical Engineering*, *44*(11), 3284–3294. https://doi.org/10.1007/s10439-016-1590-x

Otani, T., Al-Issa, A., Pourmorteza, A., McVeigh, E. R., Wada, S., & Ashikaga, H. (2016b). A computational framework for personalized blood flow analysis in the human left atrium. *Annals of Biomedical Engineering*, *44*(11), 3284–3294. https://doi.org/10.1007/s10439-016-1590-x

Paliwal, N., Ali, R. L., Salvador, M., O'Hara, R., Yu, R., Daimee, U. A., Akhtar, T., Pandey, P., Spragg, D. D., Calkins, H., & Trayanova, N. A. (2021). Presence of left atrial fibrosis may contribute to aberrant hemodynamics and increased risk of stroke in atrial fibrillation patients. *Frontiers in Physiology*, *12*(1). https://doi.org/10.3389/fphys.2021.657452

Qureshi, A., Darwish, O., Dillon-Murphy, D., Chubb, H., Williams, S., Nechipurenko, D., Ataullakhanov, F., Nordsletten, D., Aslanidi, O., & de Vecchi, A. (2020, December 30). Modelling left atrial flow and blood

coagulation for risk of thrombus formation in atrial fibrillation. *2020 Computing in Cardiology Conference (CinC)*. http://dx.doi.org/10.22489/cinc.2020.219

Sanatkhani, S., Nedios, S., Menon, P. G., Bollmann, A., Hindricks, G., & Shroff, S. G. (2021). Subject-Specific calculation of left atrial appendage blood-borne particle residence time distribution in atrial fibrillation. *Frontiers in Physiology*, *12*(1). https://doi.org/10.3389/fphys.2021.633135

Valen-Sendstad, K., & Steinman, D. A. (2013). Mind the Gap: Impact of computational fluid dynamics solution strategy on prediction of intracranial aneurysm hemodynamics and rupture status indicators. *American Journal of Neuroradiology*, *35*(3), 536–543. https://doi.org/10.3174/ajnr.a3793

Vella, D., Monteleone, A., Musotto, G., Bosi, G. M., & Burriesci, G. (2021). Effect of the alterations in contractility and morphology produced by atrial fibrillation on the thrombosis potential of the left atrial appendage. *Frontiers in Bioengineering and Biotechnology*, *9*(1). https://doi.org/10.3389/fbioe.2021.586041

Veronesi, F., Corsi, C., Sugeng, L., Caiani, E. G., Weinert, L., Mor-Avi, V., Cerutti, S., Lamberti, C., & Lang, R. M. (2008). Quantification of mitral apparatus dynamics in functional and ischemic mitral regurgitation using real-time 3-dimensional echocardiography. *Journal of the American Society of Echocardiography*, *21*(4), 347–354. https://doi.org/10.1016/j.echo.2007.06.017

Viceconti, M., Pappalardo, F., Rodriguez, B., Horner, M., Bischoff, J., & Musuamba Tshinanu, F. (2021). In silico trials: Verification, validation and uncertainty quantification of predictive models used in the regulatory evaluation of biomedical products. *Methods*, *185*(1), 120–127. https://doi.org/10.1016/j.ymeth.2020.01.011

Wang, Y., Qiao, Yonghui , Mao, Y., Jiang, C., Fan, J., & Luo, K. (2020). Numerical prediction of thrombosis risk in left atrium under atrial fibrillation. *Mathematical Biosciences and Engineering*, *17*(3), 2348–2360. https://doi.org/10.3934/mbe.2020125

Whang, W. (2018). Does left atrial appendage closure reduce mortality? A vital status analysis of the randomized PROTECT AF and PREVAIL clinical trials. *Journal of Atrial Fibrillation*, *11*(4). https://doi.org/10.4022/jafib.2119

Zhang, L. T., & Gay, M. (2008). Characterizing left atrial appendage functions in sinus rhythm and atrial fibrillation using computational models. *Journal of Biomechanics*, *41*(11), 2515–2523. https://doi.org/10.1016/j.jbiomech.2008.05.012

6 - Appendix

As mentioned in Section 3.3.1, Figure 13 shows quantitatively the mesh convergence of the hemodynamic indices. The results highlight that the desired convergence cannot be reached for coarser meshes particularly around 3 million tetrahedral elements and the convergence levels in LA and LAA were achieved by approaching the refined mesh resolutions around 7 million elements. However, the levels of mesh convergence can be reached more smoothly for LA in comparison to the results of LAA which show unstable trends and highlight more sensitivity. Furthermore, it can be observed that among the considered hemodynamic indices, OSI shows more sensitivity to meshe sizes even in LA compared to TAWSS, RRT and ECAP. Therefore, it is difficult to substantially justify OSI results for meshes below 10 million tetrahedral elements.

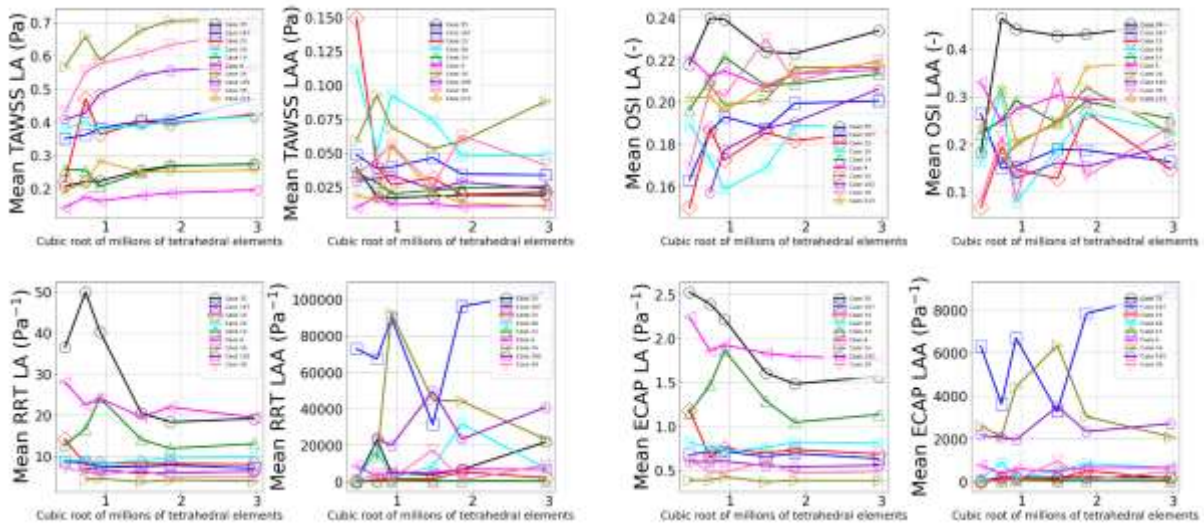

Figure 13. The impact of mesh resolutions on the mean-cycle-averaged the hemodynamic indices (i.e. TAWSS, OSI, RRT, ECAP). The results of each hemodynamic indices are separated for LA and LAA of the corresponding case. The different mesh resolutions (i.e. x-axis) are presented based on the cubic root of tetrahedral elements.

This project received funding from the European Union's Horizon 2020 research and innovation programme under grant agreement No 101016496